Dynamics of the Reaction $O(^3P) + H_2S \rightarrow OH + SH$. 2. State-Resolved Differential Cross Sections and Angular Momentum Correlations

Matthew L. Costen,† Gus Hancock,* and Grant A. D. Ritchie

Physical and Theoretical Chemistry Laboratory, Oxford University, South Parks Road, Oxford, OX1 3QZ, U.K.

Received: June 16, 1999; In Final Form: August 23, 1999

Measurements are reported of Doppler resolved polarized laser-induced fluorescence of the OH product of the $O(^3P) + H_2S$ reaction, leading to estimates of the differential cross sections and angular momentum correlations in the system. $O(^3P)$ was produced with translational energy above the barrier to reaction by the polarized 355 nm photolysis of NO_2. Three quantum states were studied in detail. For the most populated OH level, $v'' = 1$, $N'' = 6$, the scattering for the A″ Λ doublet was found to be largely sideways/backward, with the remaining energy appearing as product translation, and measurements of average Λ doublet scattering showed similar behavior for the A′ Λ doublet. The same scattering dynamics were observed for the $v'' = 0$, $N'' = 13$ state. For the rotationless $v'' = 1$, $N'' = 1$ state the results were more ambiguous, but if the same distribution of available energy appeared in the SH fragment as deduced for the measurements on rotationally excited OH, then the scattering was seen to be clearly backward. Polarization measurements of the two OH levels with $N'' > 1$ showed that the angular momentum vector **J**′ was directed perpendicular to the plane containing the relative velocity vectors of reactants and products. A model of the scattering is proposed through a planar transition state and is able to account qualitatively for these observations of the *vector* characteristics of the reaction, together with the *scalar* attributes (quantum state populations) reported in the previous paper. The model predicts that the SH coproduct will be scattered largely forward with respect to the $O(^3P)$ atom velocity, with low internal energy, and dominantly in the A″ Λ doublet.

I. Introduction

The field of reaction dynamics is evolving toward ever more detailed preparation of reagents and measurements of product final states. In the past few years new laser-based techniques have provided the opportunity to probe the products of a reaction on a quantum state resolved level and to derive their angular scattering and rotational angular momentum polarization, allowing the stereodynamics of simple bimolecular reactions to be fully elucidated. Two different strategies have been pursued. The first is the marriage of laser-based probe techniques with traditional crossed molecular beams, for example, in the reactions of $O(^1D)/S(^1D)$ with H_2 or $CN + D_2$ by Liu and co-workers.[1−4] The second involves the production of a translationally hot atom with a known velocity distribution by laser photolysis of a precursor molecule and has been pursued by a number of groups using two laser-based probe methods, polarized Doppler resolved laser-induced fluorescence (LIF), generally under "bulb" conditions,[5−20] and resonance-enhanced multiphoton ionization and time-of-flight detection (REMPI-TOF), involving coexpansion of the reagents in a molecular beam.[21−27] The earliest LIF experiments resolved only speed-averaged vector correlations,[5] but subsequently, it was shown that the laboratory velocity distribution of the products contains information about the differential scattering cross section.[6,23] Laser probing is also sensitive to the product rotational angular momentum,[28] and both the LIF and REMPI-TOF techniques have been shown to return product state resolved angular momentum differential cross sections.[29,30] Recent experimental work includes the work on $O(^1D)$ and $H(^2S)$ reactions by Brouard, Simons, and co-workers, including the full angular momentum polarization of the benchmark reaction of $O(^1D)$ with H_2.[18−20] The reaction of $H(^2S)$ with O_2 was studied at a variety of collision energies by Hall et al.[11,12] showing the opening of a different reaction geometry at the conical intersection of the $^2A_2$ and $^2B_1$ surfaces. Zare and co-workers have studied the reactions of $Cl(^2P_{3/2})$ with methanes and ethanes in great detail, producing state-to-state differential cross sections and fully resolving the available rotational polarization parameters in the production of $DCl(v'' = 0, J'' = 1)$ from the reaction with CD_4 and C_2D_6.[21,24−27]

The experiments presented in this paper represent an attempt to determine the stereodynamics of the $O(^3P) + H_2S$ reaction using polarized sub-Doppler LIF detection of the $OH(X^2\Pi)$ product. $O(^3P)$ is produced from the 355 nm photolysis of NO_2, forming atoms with their velocities aligned in the laboratory frame, and suitable combinations of photolysis and probe lasers' relative propagation vectors and polarizations allow the correlations between the velocity vectors of reagents and products and the angular momentum of the OH fragment to be determined. The results complement the product state and Λ doublet distributions reported in the preceding paper (part 1)[31] and together display how the great detail of information now available from such experiments may produce a simple coherent picture of the reactive process. The most significant result is that OH is observed to be mainly sideways-scattered, with its rotational angular momentum directed perpendicular to the scattering plane containing the relative velocity vectors of

* To whom correspondence should be addressed. E-mail: gus.hancock@chemistry.ox.ac.uk. Fax: (+44) 1865 275410.

† Current address: Chemistry Department, Brookhaven National Laboratory, Upton, NY 11973-5000.

10.1021/jp991990h CCC: $18.00
Published on Web 09/28/1999

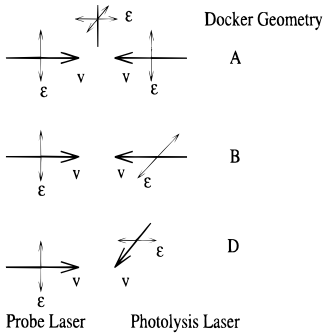

Figure 1. Experimental Docker geometries A, B, and D for the photolysis and probe lasers' propagation vectors **v** and electric vectors ϵ.

reagents and products, i.e., that it departs from the transition state with a "frisbee" type motion.

II. Experimental Section

The apparatus was described in detail in the preceding paper (part 1),[31] and only the essential differences are noted here. The experiments were performed in the same reaction cell as before, with equal partial pressures of 50 mTorr of NO_2 and H_2S. The photolysis laser beam was propagated relative to the probe laser and detection axes in three geometries, as defined by Docker[32] as A, B, and D and shown in Figure 1. The product OH($X^2\Pi$) was probed using LIF via the A−X transition on the (0, 1), (0, 0) and (1, 1) bands. Probing on the (0, 1) band used LDS698 dye in methanol, while probing on the (0, 0) and (1, 1) bands used DCM dye in MeOH. The probe laser bandwidth was narrowed by insertion of an intracavity etalon with a free spectral range of 10 GHz and a finesse of 14. The resulting time-averaged bandwidth in the fundamental was measured to be 0.025 cm^{-1} using a spectrum analyzer (Burleigh PLSA). The fundamental frequency was then doubled in KD*P to give radiation in the region 340−345 nm for probing the (0, 1) band and in the 310−316 nm region for probing transitions in the (0, 0) and (1, 1) bands. The probe fluence was more than sufficient to saturate main branch transitions in the strong diagonal bands and was accordingly attenuated using crossed polarizers. The absence of saturation was confirmed by the linearity of signal with probe fluence, and the ratio of main to subbranches agreed with the calculated transition probabilities. In addition the form of the Doppler profiles was invariant to laser fluence in the regime used, ≤ 40 μJ cm^{-2}. Spectra were recorded in scans of 1.32 cm^{-1} in the ultraviolet to ensure a clean baseline on either side of the Doppler profile, typically with 30 laser shots per point, with 300 points covering a transition.

III. Probe Laser Bandwidth

The shape of the measured Doppler profiles includes a contribution from the form of the laser bandwidth, and an accurate knowledge of this is essential for successful analyses of the results. The laser spectral profile may be obtained by deconvoluting the contribution it makes to a known spectral line shape, in this case a translationally thermalized OH transition, provided by OH from a microwave discharge (EMS Microtron 2.45 GHz) in room-temperature H_2O/Ar. The true OH line shape is a Gaussian within the resolution of the experiment, and the Doppler profile recorded by scanning the probe laser over this transition will be a convolution of the Gaussian and the probe laser spectral line shape.

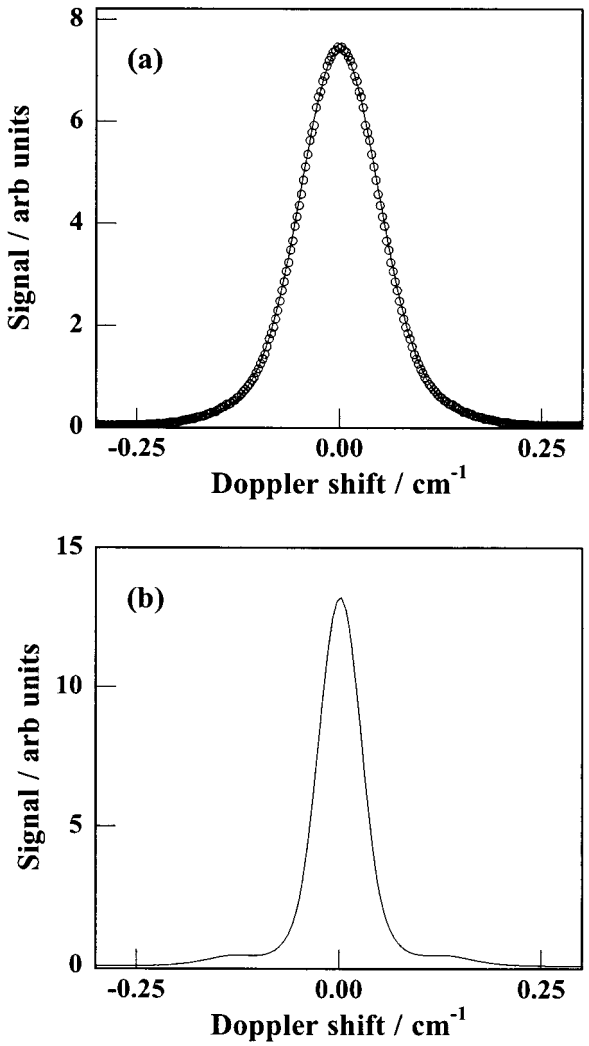

Figure 2. Measurements of the probe laser bandwidth on the $P_{12}(8)$ transition of the (0, 0) band of OH at 298 K. Part a shows the experimental LIF profile (points) together with the fit to the data as explained in the text. Part b shows the laser spectral profile deconvoluted from the fit to the data.

Deconvolution may in principle be made by Fourier transform methods, but these are extremely sensitive to noise in the input data and are not constrained to produce physically realistic results. Instead, the probe laser bandwidth was determined using an iterative constrained nonlinear deconvolution.[33] In this approach the known Gaussian transition line shape is convoluted by a Fourier transform method with a response function and a starting guess at the laser line shape, and the result is compared with experimental results. The response function, initially chosen for convenience to be the measured line shape, is then altered to reduce the deviation from the experimental result, and the process is repeated. At each step the response function is constrained to be positive and is smoothed using a Fourier transform low-pass filter. The process is repeated until the χ^2 values indicate that the result has converged, at which point the response function represents the laser spectral profile. Figure 2 shows an average of nine experimental scans across the P_{12}-(8) transition of the (0, 0) band together with the fitted result from the deconvolution, and Figure 2b shows the resultant deconvoluted line shape. The fwhm, 0.06 cm^{-1}, is a little over twice that of the fundamental bandwidth as measured by the spectrum analyzer, and the broad pedestal is thought to arise from incomplete suppression of the unnarrowed bandwidth by

the etalon. The bandwidth should be compared with the smallest Doppler widths measured in these experiments, ~0.2 cm^{-1}, and as will be shown later, the precision in the differential cross sections extracted from such data is dependent on a knowledge of the laser bandwidth.

IV. Differential Cross Sections from Doppler Profiles

A. Velocity-Dependent Correlations. The basic principle behind the determination of differential cross sections from photoinitiated bimolecular reactions was originally elucidated by Shafer et al.,[23] and the analysis used in the present work is similar to those described by Brouard[6] and Hall.[11,12] We define the LAB frame of reference as that in which the electric vector of the photolysis laser forms the *z* axis, and the hot atom A in the reaction

$$A + BCD \rightarrow AB + CD \quad (1)$$

has a velocity $\mathbf{v_A}(v_A,\theta_A,\phi_A)$ with an angular dependence defined by the photodissociation through the translational anisotropy factor (the distribution of the values of θ_A, the angle between $\mathbf{v_A}$ and the *z* axis). In the LAB frame a given value of v_{AB}, the speed of the AB product, results in a Doppler profile that has the form[5,6]

$$D(v_p) = \frac{1}{2v_{AB}}\left[g_0(v_{AB}) + g_2(v_{AB})P_2\left(\frac{v_p}{v_{AB}}\right) + g_4(v_{AB})P_4\left(\frac{v_p}{v_{AB}}\right)\right]; \quad -v_{AB} < v_p < v_{AB} \quad (2)$$

Here, v_p is the measured LAB frame Doppler velocity projection, and P_2 and P_4 are Legendre polynomials. The g_i are functions that contain geometrical terms, dependent on the experimental geometries (the Docker cases described in Figure 1), on the particular type of transition being excited (P, Q, or R branches) and observed (all possible branches in the present experiments), and on the bipolar moments of the vectors describing the velocities and angular momenta of reactants and products. The last correlations are the results that we seek.

We measure Doppler profiles in the LAB frame, whereas the scattering takes place in the center-of-mass (CM) frame. Direct inversion of the LAB frame product velocity distribution to give the CM distribution is impractical, since the frame transformation and initial distributions of parent velocities preclude a unique solution. However, forward simulation of a LAB frame Doppler profile is straightforward for a given CM scattering distribution and is described in detail in the Appendix. To extract the scattering dynamics from the experimental data, we take appropriate linear combinations of profiles taken with different geometries and rotational branches.[32] We construct two LAB frame "composite profiles", which we refer to as $D_0^0(0,0;v_p)$ and $D_0^2(2,0;v_p)$. These form respectively a "top-hat" profile dependent purely on the speed of the product in the LAB frame, and a profile whose width is dependent on the speed and whose shape is dependent on θ_u, where θ_u is the CM angle between the velocity vectors $\mathbf{k}$ and $\mathbf{k}'$ and gives information on the differential cross section. These composite profiles are formed from sums and differences of the Doppler profiles at various Docker geometries (A + B + D for $D_0^0(0,0;v_p)$, the average of A − D and B − D for $D_0^2(2,0;v_p)$; see Appendix), and it can be seen that data of high precision are needed to extract the differential cross section from differences in observed line shapes. We can thus form composite Doppler profiles for any CM speed and scattering angle and for any combination of the initial velocities of the reagents.

Composite Doppler profiles for use as basis functions in the backfitting of experimental data have been formed in the following fashion. Velocities were selected by a Monte Carlo method from the initial velocity distribution of the $O(^3P)$ atom and the target H_2S molecule thermal velocity distribution. For given initial and final states it is possible to calculate the available energy that can be released as translational energy in the CM frame. In an A + BC reaction this will result in a single possible product CM speed, whereas in the current system energy may be partitioned into the internal degrees of freedom of the coproduct SH. A set fraction of the available energy, F_T, is thus assumed to be partitioned into product translation for each basis function in this case. A single polar scattering angle θ_u is chosen, while the azimuthal scattering angle is selected from a uniform distribution. Composite Doppler profiles $D_0^0(0,0;v_p)$ and $D_0^2(2,0;v_p)$ can be generated using the relations listed in the Appendix. This procedure is repeated iteratively until the results have converged; they are then averaged and convoluted with the experimentally determined laser line shape function. A full array of basis functions spanning the space of the CM scattering angle θ_u and fraction of available energy released in translation F_T may thus be formed by repeating this procedure for the different values of these parameters.

B. Fitting Doppler Profiles. The experimental data are assumed to be formed from a linear combination of the constructed basis sets, and thus, a suitable fitting routine is needed to return the differential scattering cross section and translational energy release. Several different fitting methods have been explored and have been found to produce equivalent results for the determination of $P(\cos\theta_u)$ and $P(F_T)$, and two of these are presented here. The first assumes that the distributions of the two parameters are separable and can be represented by

$$P(F_T) = F_T^{\,a}(1 - F_T)^b \quad (3)$$

$$P(\cos\theta_u) = (\cos\theta_u)^c(1 - \cos\theta_u)^d \quad (4)$$

where $\cos\theta_u$ has been rescaled to range from 0 to 1. These functional forms have the flexibility to represent plausible physical distributions while suppressing unreasonable oscillations and enable the complete scattering angle and energy distribution to be described by four variables *a*, *b*, *c*, and *d*. The four-dimensional parameter space of this representation has been searched for a χ^2 minimum using a simplex algorithm.[34] At each iteration of the algorithm trial values of the variables *a*−*d* were used to construct trial composite Doppler profiles $D_0^0(0,0;v_p)$ and $D_0^2(2,0;v_p)$ subject to the constraints that the probabilities be positive and sum to unity. These trial profiles were then used to evaluate their χ^2 with the Doppler profile data. Restarting the algorithm in disparate regions of the parameter space confirmed that the χ^2 minimum found was not purely a local minimum. We call this fitting routine the separable variable method (SVM).

The second method, used by several groups previously,[7,11,21] is that of singular value decomposition (SVD). The basis sets for the two composite Doppler profiles were fitted simultaneously to the experimental data, providing a rigorous least-squares answer. This fitting procedure assumes that the differential cross section and F_T distribution are nonseparable. After the SVD procedure has been applied to the basis set a series of linear combinations of the basis functions are returned, along

with a weighting vector. Unphysical oscillations in the returned differential cross section were suppressed by taking only those combinations returned with a weight that is >5% of the maximum. The combinations taken are then backfitted to the data to return the appropriate coefficients. Increasing the number of combinations taken did not significantly increase the χ^2 of the fit. The SVD routine does not apply the physical constraints of positive probability and sum to unity on the fitted distributions. A simulated annealing, or maximum entropy, procedure was also tried, and the results from this were not significantly different from those given by the SVD routine.

C. Angular Momentum Correlations. The Doppler profiles are also dependent on the correlated distributions of velocity and angular momentum vectors, represented by the bipolar moments excluded in the composite profiles $D_0^0(0,0;v_p)$ and $D_0^2(2,0;v_p)$ used for differential cross section determination. Polarized angular momentum differential cross sections have been formalized and their treatment and measurement extensively described both for REMPI-TOF experiments and LIF Doppler profiles.[29,30] The angular momentum correlations have generally significantly smaller overall effects on the Doppler profile line shape, and such a detailed analysis requires exceptionally high-quality data. The relatively low signal to noise, coupled with the poor initial definition of the system, precluded a detailed analysis in this experiment. The angular momentum correlations have instead been treated in a semiclassical fashion via an extension of the Monte Carlo forward simulation technique used for the differential cross sections, and the details are described in the Appendix. An assumed angular momentum distribution is used to generate composite Doppler profiles. The same procedure is used as for the differential cross sections, with the addition of the selection of the CM angular momentum angles for each scattering angle and fraction of available energy in translation. Simulations of the experimental data can then be formed using the measured differential scattering cross section and energy distribution.

V. Results

Doppler profiles need to be taken for the three Docker geometries A, B, and D, probing Q, P, and R branches in order to eliminate angular momentum effects, but for the OH A−X transition there is an additional complication in that the strong Q, P, and R branches (those with $\Delta J = \Delta N$) probe opposite Λ doublets (for example, Q_{11} probes the A″, P_{11} and R_{11} each probe the A′). This can often be overcome by measurements of both the main and satellite lines originating from the same Λ doublet level (e.g.,, the Q_{11} and P_{21} lines), which are split by the spin rotation doubling in the upper $^2\Sigma$ state. In the present work this has not always been possible as explained below, and in one case Λ doublet averaged vector correlations have been measured.

A. Averaged Rotational Alignment. The construction of the composite Doppler profiles requires that the profiles taken at different geometries and on different branches be correctly normalized to one another, and this needs to take into account any rotational alignment in the LAB frame and the angular momentum coupling and geometrical factors. This can be done by integrating the area of the whole Doppler profile and renormalizing such that the integral intensity is given by

$$I = b_0 + b_1 \frac{4}{5} A_0^{(2)}(\mathrm{LAB}) \qquad (5)$$

where the b_n premultipliers are as defined in the Appendix and

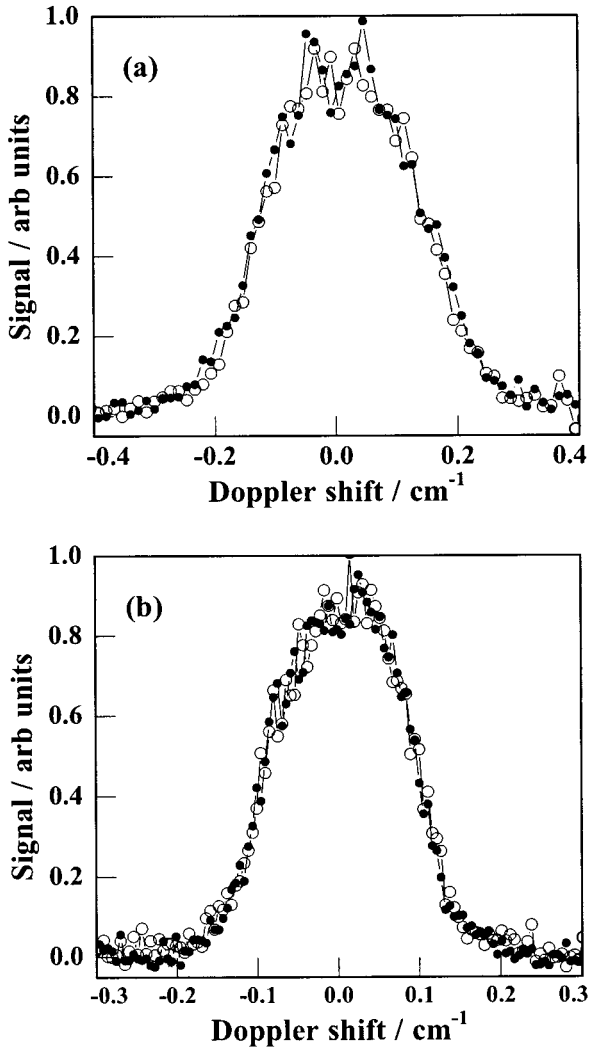

Figure 3. Examples of single-scan Doppler profiles taken in Docker geometries A (filled circles) and B (open circles) for the $P_{22}(13)$ line of OH taken on the (0, 0) band (a) and the $Q_{11}(6)$ line taken on the (0, 1) band (b). Average rotational alignments for use in normalizing the Doppler profiles were calculated from the integral areas of multiple scans and are given in Table 1.

$A_0^{(2)}$(LAB) is the LAB frame averaged rotational alignment of the product OH with respect to the LAB frame *z* axis, the electric vector of the photolysis laser. $A_0^{(2)}$(LAB) may be conveniently measured by recording the integral intensity of the transition for two orthogonal polarizations of the photolysis laser, using the experimental Docker geometries defined as A and B in Figure 1. The measurements were made during the same scan by rotating the polarization of the photolysis laser with an electrooptic switch, a KD*P crystal across which 3.2 kV was applied. This technique does not suffer from beam walk and avoids systematic errors caused by slow drifts in experimental conditions. Our measured vector correlations have concentrated on three levels, namely, both A′ and A″ Λ doublets of the $v'' = 1$, $N'' = 6$, F_1 state and the $v'' = 0$, $N'' = 13$, F_2, A′ Λ doublet. The average rotational alignments for these three levels were measured from the integral areas of Docker A and B geometries probed by the $R_{11}(6)$ and $Q_{11}(6)$ transitions of the (0, 1) band, and the $P_{22}(13)$ transitions of the (0, 0) band, respectively. Examples of single switched scans of the $Q_{11}(6)$ and $P_{22}(13)$ transitions are shown in Figure 3 and indicate the relatively low signal-to-noise ratio for a single scan. A test of any systematic bias in the alignment of the laser beam or in the

TABLE 1: Measured Areas for Doppler Profiles Taken at Geometries A and B, with the Extracted LAB Rotational Alignment Factors $A_0^{(2)}$(LAB)[a]

transition	A/B ratio	$A_0^{(2)}$(LAB)	integral A	integral B & D
$Q_{12}(1)$, $v = 1$, A′			1.000	1.000
$R_{11}(6)$, $v = 1$, A′	0.999 ± 0.010	0.002 ± 0.016	1.060 ± 0.011	1.060 ± 0.006
$Q_{11}(6)$, $v = 1$, A″	0.954 ± 0.015	-0.029 ± 0.010	0.874 ± 0.010	0.916 ± 0.005
$P_{21}(6)$, $v = 1$, A″			1.062 ± 0.006	1.028 ± 0.003
$P_{22}(13)$, $v = 0$, A′	1.041 ± 0.012	-0.04 ± 0.011	1.077 ± 0.008	1.033 ± 0.004
$Q_{12}(13)$, $v = 0$, A′			0.852 ± 0.011	0.912 ± 0.005

[a] The final two columns give the normalization factors for the areas measured for geometries A, B, and D calculated via eq 5. The quoted errors are 2σ from the results of multiple scans of the type shown in Figure 3.

fluorescence imaging system can be made by recording the integral intensities from switched scans of the $Q_{12}(1)$ transition, which cannot display a LAB frame rotational alignment.[28] These measurements were made both on the (1, 1) band with product from the O + H_2S reaction and on the (0, 0) band with product from the 355 nm photolysis of HONO and showed no such bias, yielding an average A/B ratio of 0.999 ± 0.007.

The results of all the measurements are given in Table 1, where the resulting integral areas in the three experimental geometries used for normalization of the experimental Doppler profiles are given with 2σ errors from multiple scans of the type shown in Figure 3. The results for the $v'' = 1$, $N'' = 6$, F_1, A″ and the $v'' = 0$, $N'' = 13$, F_2, A′ states both show small negative LAB frame alignments, while the $v'' = 1$, $N'' = 6$, F_1, A′ state shows no alignment within the experimental precision. Dramatically different polarization dynamics for states differing only in electronic orbital alignment have been seen before.[11,13] In each of these cases the polarization was lost on the less populated of the Λ doublets and was assumed to be the result of exit channel effects after the reaction had proceeded on a single surface. In the present case the A′ Λ doublet is the major channel,[31] and the $P_{22}(13)$ transition, which also probes the A′ Λ doublet, shows the strongest alignment. The lack of a LAB frame rotational alignment does not necessarily imply a lack of a center of mass frame polarization because of the frame transformations and averaging effects in the experimental system, but the different LAB frame alignments, if significant, do imply either different polarization dynamics or different translational scattering dynamics. This point is discussed in section C below. We finally note that the A/B measured ratios shown in Table 1 are close enough to unity to allow rotational state distributions to be determined (and reported in the preceding paper[31]) without correction for the rotational alignment.

B. Differential Scattering Cross Sections. Doppler profiles were acquired for three different v'', N'' quantum states of the OH product.

(1) The first is the peak of the rotational distribution in $v'' = 1$, namely, $N'' = 6$ in the F_1 spin−orbit manifold. Doppler profiles were acquired in two ways. First, the $Q_{11}(6)$ and its satellite $P_{21}(6)$ were recorded on the (1, 1) band resulting in differential cross sections for the $N'' = 6$ A″ Λ doublet. Unfortunately, the more populated A′ state could not be probed because of blending in the required $R_{11}(6) + Q_{21}(6)$ lines. Correspondingly, measurements were made on the $N'' = 6$ level probed in the (0, 1) band, but here another problem arose: although good data could be taken on the strong $R_{11}(6)$ and $Q_{11}(6)$ lines (probing A′ and A″ levels, respectively) the corresponding satellite lines ($Q_{21}(6)$ and $P_{21}(6)$) were too weak to be recorded with the precision required. Thus, although we present the fully resolved data on the A″ level, the only information that we have on the A′ level must be inferred from the Λ *doublet averaged* data. The LAB frame rotational alignment measurements demonstrated the possibility of different scattering dynamics in the two Λ doublets, and thus we need to treat these averaged data with care.

(2) A high rotational state of the ground vibrational level was probed, the $v'' = 0$, $N'' = 13$, F_2, A′ state via the $P_{22}(13)$ and $Q_{12}(13)$ transitions of the (1, 1) band. The preceding paper[31] shows that OH $v'' = 0$, $N'' \leq 6$ is produced in the NO_2/H_2S system as a result of the photolysis of HONO, a seemingly unavoidable contaminant. Furthermore, levels up to $N'' = 12$ are formed by energy transfer from internally excited NO (produced from the 355 nm photolysis of NO_2) into the OH product of HONO photolysis. $N'' = 13$, however, was found to be a nascent product from the O + H_2S reaction only.

(3) Finally, the lowest rotational state, $N'' = 1$, F_2, A′ was probed for $v'' = 1$. The rotational angular momentum of this state can only be oriented, not aligned,[28] and the only effects on the shape of the Doppler profiles measurable with the linearly polarized light used in this study are from the differential cross section and translational energy release. Doppler profiles are thus only required from one branch and were acquired via the $Q_{12}(1)$ transition of the (1, 1) band.

Multiple Doppler profiles (6−10) of each transition were recorded at each geometry and were averaged to improve the signal to noise. In all cases the profiles were taken over the full line shape and *not* symmetrized. The averaged profiles were then renormalized to the correct integral areas as given in Table 1. The composite Doppler profiles $D_0^0(0,0;v_p)$ and $D_0^2(2,0;v_p)$ were then constructed using these averaged profiles and the relevant angular momentum coupling factors as described in Table 2. The data from the $Q_{11}(6)$ and $R_{11}(6)$ transitions probed on the (0, 1) band were also used to construct composite Doppler profiles, averaging the LAB frame rotational alignments measured for these two states.

Basis functions were then calculated for each quantum state using the Monte Carlo simulation program described above. The exothermicity of the reaction[35] was taken as -49.4 kJ mol^{-1}, and the OH state energies were taken from the data of Dieke and Crosswhite.[36] The O(^{3}P) velocity distribution was represented by two equally weighted Gaussians with standard deviations of 200 ms^{-1} and centered on 980 and 1600 ms^{-1}, with the translational anisotropies β set to 0.46 and 0.66, respectively.[10] Recent measurements in this laboratory of the NO quantum state dependent β values in the 355 nm photolysis of NO_2 suggest that the O(^{3}P) anisotropy will be speed-dependent, but the bulk of the distribution, particularly for the high-velocity atoms, which will have sufficient energy to surmount the barrier, is well represented by these values.[37] The probe laser bandwidth was taken as the deconvoluted function shown in Figure 2b. The basis functions were then calculated as an evenly spaced grid in scattering angle, $\cos\theta_u$, and as a fraction of available energy released into translation, F_T, with 11 values in each parameter and with 10^5 iterations of the Monte

TABLE 2: Terms in the Composite Constructions[a]

	composite construction	resulting profile
1	$(^1/_3)(A + B + D)^P q_Q^{(2)} - (^1/_3)(A + B + D)^Q q_P^{(2)}$	$D_0^0(0,0;v_p) = \frac{f}{2v_{AB}}$
2	$(A - D)^P q_Q^{(2)} - (A - D)^Q q_P^{(2)}$	$D_0^2(2,0;v_p) = -\frac{3f\beta_{v_A}(v_A)}{4v_{AB}}\beta_{v_A v_{AB}}(v_{AB})\,P_2\left(\frac{v_p}{v_{AB}}\right)$
3	$(B - D)^P q_Q^{(2)} - (B - D)^Q q_P^{(2)}$	$D_0^2(2,0;v_p) = -\frac{3f\beta_{v_A}(v_A)}{4v_{AB}}\beta_{v_A v_{AB}}(v_{AB})\,P_2\left(\frac{v_p}{v_{AB}}\right)$
4	$(^1/_3)(A + B + D)^P q_Q^{(0)} - (^1/_3)(A + B + D)^Q q_P^{(0)}$	$D_0^0(2,2;v_p) = \frac{f\beta_{v_{AB}J}(v_{AB})}{2v_{AB}}P_2\left(\frac{v_p}{v_{AB}}\right)$
5	$(A - D)^P q_Q^{(0)} - (A - D)^Q q_P^{(0)}$	$D_0^2(0,2;v_p) = -\frac{f}{2v_{AB}}\frac{\beta_{v_A}(v_A)}{2}\left(\frac{6}{5}\beta_{v_A J}(v_{AB}) + \frac{9}{5}\beta_{v_A{}^2 v_{AB}J}(v_{AB})\,P_4\left(\frac{v_p}{v_{AB}}\right)\right)$
6	$(B - D)^P q_Q^{(0)} - (B - D)^Q q_P^{(0)}$	$D_0^2(2,2;v_p) = \frac{f}{2v_{AB}}\frac{\beta_{v_A}(v_A)}{2}\left(\frac{12}{7}\beta_{v_A v_{AB}J}(v_{AB})\,P_2\left(\frac{v_p}{v_{AB}}\right) - \frac{9}{7}\beta_{v_A{}^2 v_{AB}J}(v_{AB})\,P_4\left(\frac{v_p}{v_{AB}}\right)\right)$

[a]The sum or difference of profiles taken on the same rotational branch are listed, for example, in the form $(A - D)^Q$, signifying the difference of the geometry A and D profiles on a Q branch. The $q_Q^{(n)}$ are the angular momentum coupling terms defined in ref 32, suitably weighted and averaged to account for emission over multiple branches. The resulting profiles include the factor $f = (q_P^{(0)} q_Q^{(2)} - q_Q^{(0)} q_P^{(2)})$ and $\beta_{nm}(v_{AB})$, the bipolar moments defined by the moving frame vector correlations. Profile 1 is dependent simply on the speed of AB, the "top-hat" profile described in the text. Profiles 2 and 3 give the same information, namely, $\beta_{v_A v_{AB}}(v_{AB})$, which is dependent on the magnitude of θ_u, the CM scattering angle, and hence yields information on the differential cross section. Profiles 4−6 contain angular momentum dependent bipolar moments that will yield information on the product angular momentum polarization.

Carlo selection procedure performed for each element of the array. The reaction has a barrier estimated[38] at 14.2 kJ mol^{-1}, and the effect of introducing the barrier as a step function in the reaction probability was to increase the apparent anisotropy of the O(^{3}P) velocity distribution. The overall effect on the basis functions was small, and no significant changes in the fitted differential cross sections were found on including the barrier in this fashion. The basis functions were assumed to be insufficiently sensitive to the barrier for more complicated functions to be justified.

The basis functions were then fitted to the composite Doppler profiles using the two different fitting procedures described previously. The SVD fits were truncated to the first five or six singular values, those with weights >5% of the maximum. Inclusion of lower weighted components did not significantly improve the returned χ^2 but introduced unphysical oscillations into the distributions. The errors shown on the SVD fits come directly from the covariance matrix of the SVD procedure and are shown as 2σ confidence limits.

The composite Doppler profiles and fitted functions for the $v'' = 1$, $N'' = 6$, F_2, A″ Λ doublet probed on the (1, 1) band and those for the averaged Λ doublets probed on the (0, 1) band are shown in Figure 4. The returned differential cross sections and translational energy releases are shown in Figure 5 for both probing and fitting schemes. In each case the unconstrained SVD fit shows some unphysical negative excursions but overall shows the same general form as the much more tightly constrained SVM fit. The SVD distributions have been summed to provide integral differential cross sections over the translational energy and the energy distribution integrated over the scattering angle, since no significant variations were seen in the differential scattering cross section with translational energy release. The major conclusion from these data is that the product in each case is seen to be scattered predominately sideways but with an asymmetry toward backward, with the translational energy distribution peaking at the maximum energy in product translation.

The results for the $v'' = 0$, $N'' = 13$, F_2, A′ state are shown in Figure 6. The returned differential cross section is found again to be sideways/backward scattered with the available energy partitioned predominately into reagent translation, and again, there was no significant variation in the differential cross section with the energy release.

The results for the $v'' = 1$, $N'' = 1$, F_2 state are more equivocal. The signal to noise was poorer for this state because of its relatively low population, and the fitting routines returned the results shown in Figure 7. The differential cross section appears to be more broadly isotropic with significant energy released into SH product rotation. A closer examination of the basis functions reveals, however, an ambiguity for this energy release: forward-scattered products with low translational energy produce profiles similar to profiles of backward-scattered products with high translational energy. Simulations showed that the fitting routines were unable to distinguish between these two cases even with noiseless data and illustrate the problems associated with the analysis of Doppler profiles when the cofragment has internal energy levels. Accordingly, an assumption was made that the translational energy release was similar to that observed for the two previously determined states, and the basis functions were contracted across suitable energy release distributions. These contracted functions were then fitted to the data, and the result shown in Figure 8 yields a χ^2 value similar to that of the unconstrained fits of Figure 7 but now with a dominantly backward-scattered differential cross section. Clearly, the results are ambiguous and must be interpreted with the help of the other dynamical information obtained about the reaction.

The overall shape of the distributions shown for the $v'' = 1$, $N'' = 6$, and $v'' = 0$, $N'' = 13$ states is thought to be well determined because the qualitative shape of the $D_0^2(2,0;v_p)$ profiles could only be reproduced for product scattered sideways in the CM frame with a speed that is near that corresponding to the maximum available translational energy. As an example of the magnitude of the variation of the composite profiles brought about by changes in the scattering dynamics, we show in Figure 9 the calculated $D_0^0(0,0;v_p)$ and $D_0^2(2,0;v_p)$ functions for fully forward and fully backward scattering in OH $v'' = 0$, $N'' = 13$ (in this case with F_T constrained to the form shown in Figure 6). The extreme cases should be compared with the best fit (for sideways/backward scattering) shown in Figure 6. The marked differences are the result of favorable kinematics of this

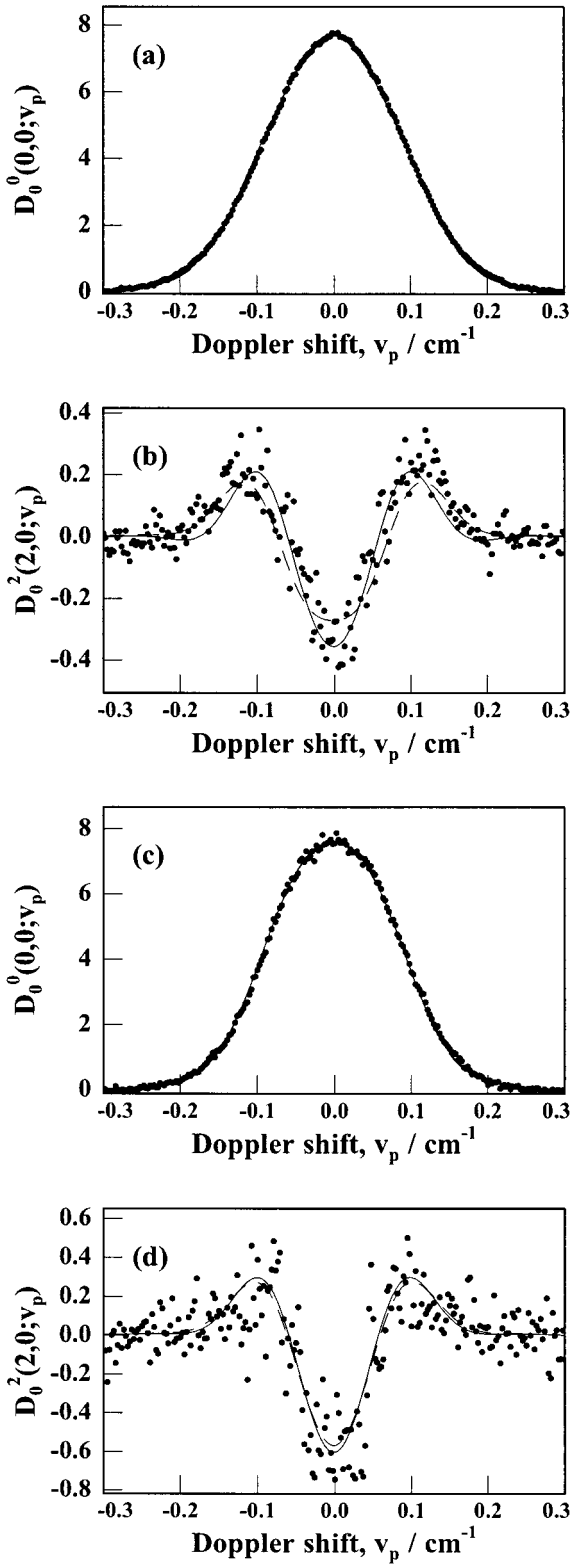

Figure 4. Experimentally derived composite Doppler profiles of nascent OH (filled circles) together with their fits from the unconstrained SVD method (solid lines) and the constrained SVM method (dashed lines). In parts a and b the composite profiles $D_0^0(0,0;v_p)$ and $D_0^2(2,0;v_p)$ are shown for the $v'' = 1$, $N'' = 6$, F_1, A″ level, probed in the (1, 1) band, and in parts c and d these profiles are shown for the Λ doublet averaged levels in the $v'' = 1$, $N'' = 6$, F_1 state.

reaction at this collision energy and give us good confidence in the broad conclusions of the scattering dynamics.

C. Angular Momentum Correlations. The full description of the angular momentum correlations in the CM frame provides

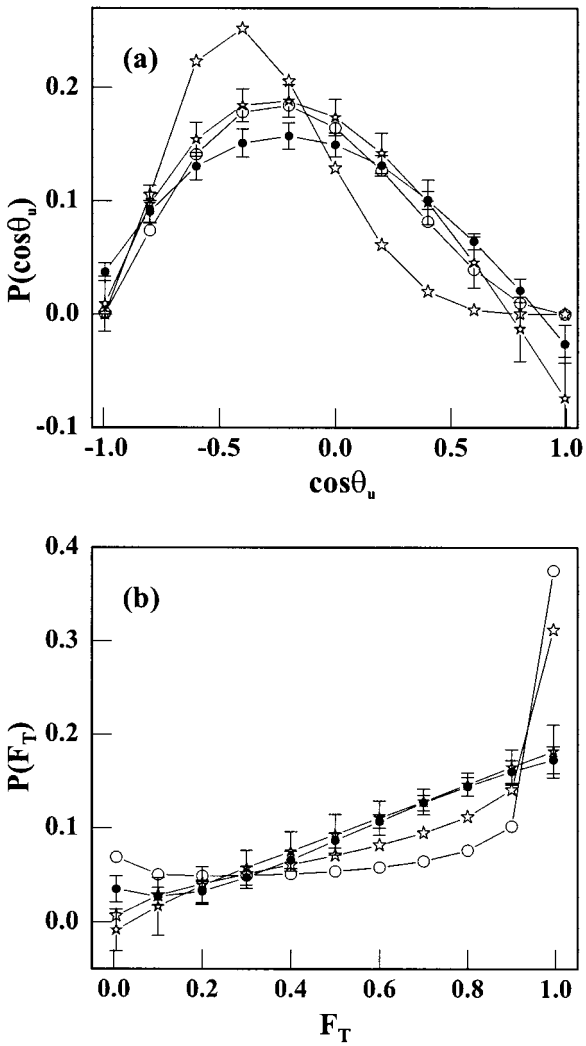

Figure 5. Differential cross sections $P(\cos\theta_u)$ (a) and fraction of available energy appearing in translation, $P(F_T)$ (b). Data are for the $v'' = 1$, $N'' = 6$, F_1, pure A″ Λ doublet probed on the (1, 1) band (filled circles, SVD fit; open circles, SVM fit) and for the $v'' = 1$, $N'' = 6$, F_1 averaged Λ doublet probed on the (0, 1) band (small stars with error bars, SVD fit; large stars, SVM fit). In all cases the scattering is seen to be sideways ($\cos\theta_u \approx 0$), with an asymmetry toward the backward ($\cos\theta_u < 0$) rather than forward ($\cos\theta_u > 0$) hemisphere. Both sets of fits produce essentially the same scattering, with the unconstrained SVD fit showing unphysical negative values for the differential cross section for $\cos\theta_u$ close to unity.

a daunting problem for an attempt at forward simulation. A complete description of the angular momentum polarization would require $2J(J+1) - {}^1/_2$ polarization-dependent differential cross sections for each value of the F_T distribution,[29] and clearly some simplifying assumptions must be made if we are to proceed. The first assumption that has been made is that the angular momentum polarization is independent of the cofragment internal energy. This is justified on the sharply peaked translational energy distribution for the reaction and the invariance of the differential scattering angle cross section with translational energy, both of which indicate a single scattering mechanism. The second assumption is that the angular momentum polarization is independent of scattering angle; i.e., the polarization-dependent differential scattering cross sections are isotropic. The dominately sideways scattered differential cross sections do suggest a single scattering process, unlike, for example, the forward/backward scattering observed in the H +

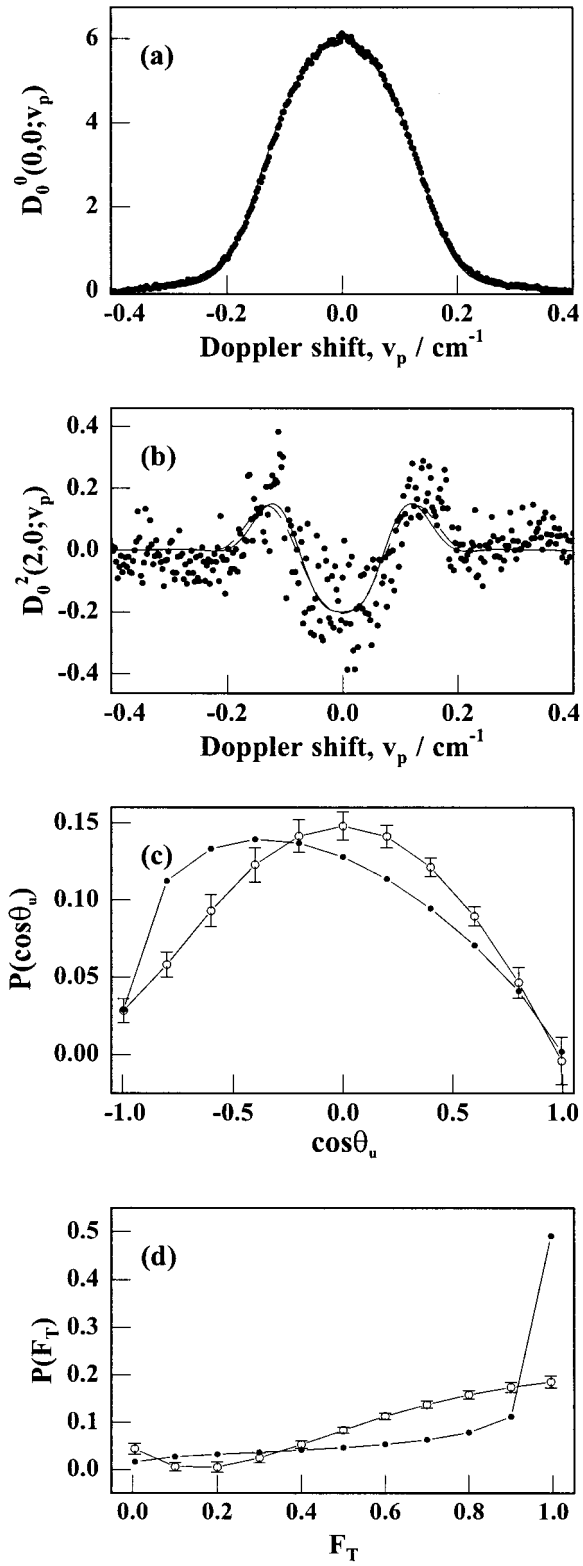

Figure 6. Composite Doppler profiles and returned differential cross sections and distributions of translational energy for the $v'' = 0$, $N'' = 13$, F_2, A′ state of OH. Parts a and b show the experimental data, together with the SVD (solid lines) and SVM (dashed lines) fits. Part c shows the differential cross sections for the two fitting methods, SVD (open circles with representative error bars) and SVM (filled circles), and part d shows the corresponding distributions of the fractional available energy in translation, F_T. Scattering dynamics are very similar to those for the $v'' = 1$, $N'' = 6$ states shown in Figure 5.

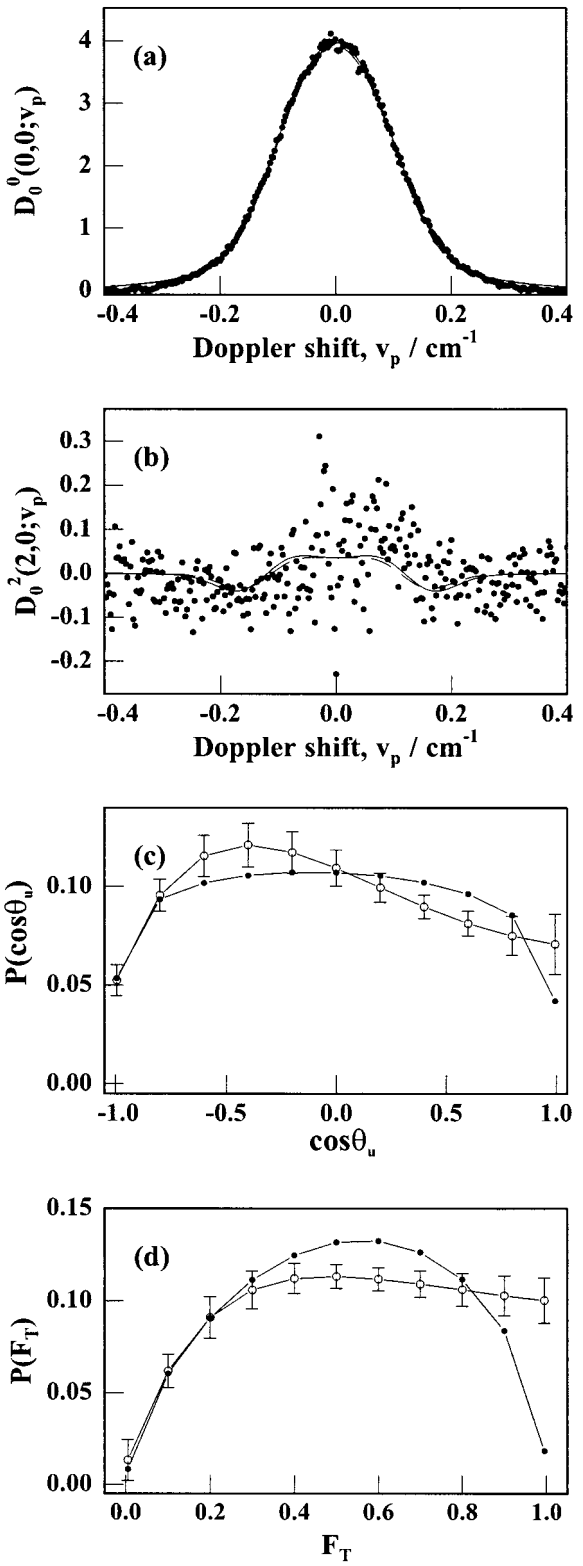

Figure 7. Composite Doppler profiles and returned differential cross sections and distributions of translational energy for the $v'' = 1$, $N'' = 1$, F_2, state of OH. Parts a and b show the experimental data, together with the SVD (solid lines) and SVM (dashed lines) fits. Part c shows the differential cross section and part d the distribution of fractional translational energy for the SVD (open circles) and SVM (filled circles) methods. As explained in the text, the fitting routines yield ambiguous results.

CO_2 reactions where the angular momentum polarization was found to vary markedly with scattering angle.[13]

There are three simple limiting cases of the relationship of the rotational angular momentum to the scattering plane that may have obvious dynamical significance. In each case the *z*

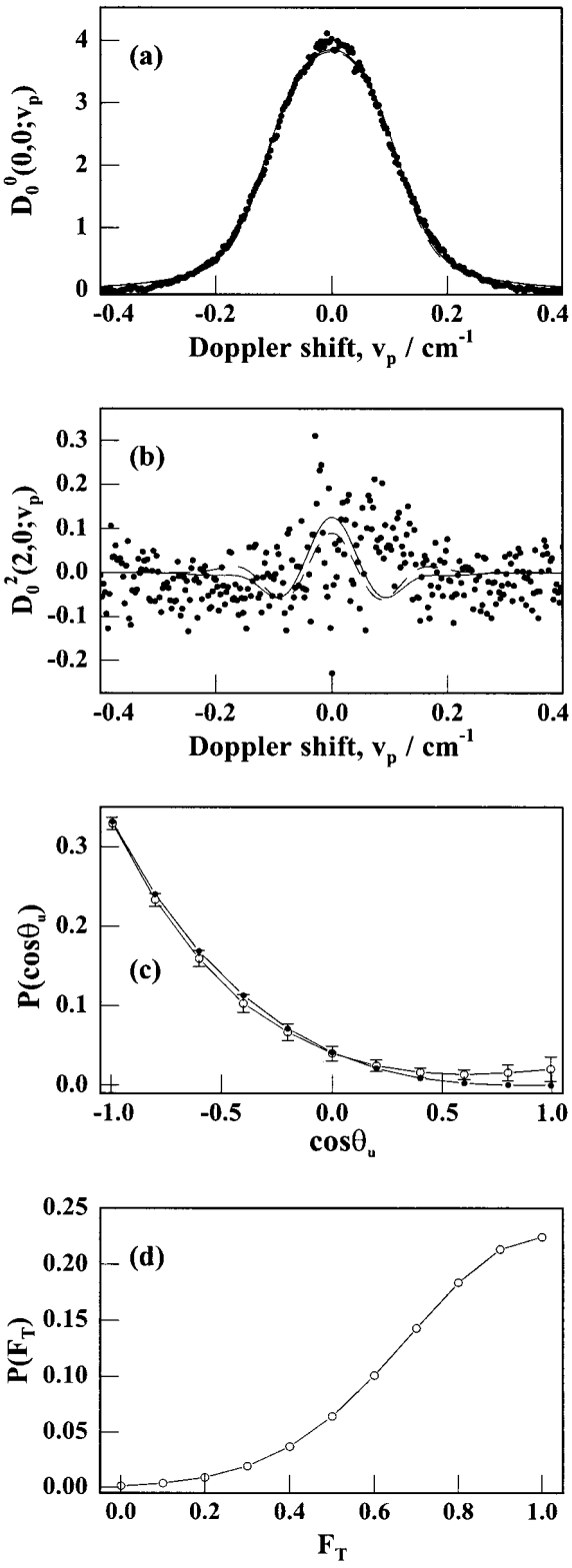

Figure 8. Composite Doppler profiles, fits, and returned differential cross section for the $v'' = 1$, $N'' = 1$, F_2 state of OH when the distribution of F_T is constrained to be similar to that deduced for the other levels measured. Parts a and b show the composite profiles and their fits, indicating qualitatively little difference from the unconstrained fits in parts a and b of Figure 7. Part c (open circles, SVD fit; filled circles, SVM fit) shows the returned differential cross section to be backward-scattered when the distribution of F_T has the assumed form shown in part d.

axis may be considered to be the product scattering direction, **k′**, with the scattering plane containing the **k** and **k′** vectors. In the classical limit of high angular momentum the three limiting cases are the "propeller" motion, with **J′**||**k′** and in the **k,k′** plane, the "cartwheel" with **J′**⊥**k′** and in the **k,k′** plane, and the "frisbee" with **J′**⊥**k′** and perpendicular to the **k,k′** plane. Simulations for these three cases have been performed assuming the following angular distributions of the angular momentum. For the propellor a $\cos^2\theta$ distribution of the **J′** vectors relative to **k′** was assumed with azimuthal symmetry. The cartwheel and frisbee both have a $\sin^2\theta$ distribution of **J′** relative to **k′** but respectively have $\cos^2\phi$ and $\sin^2\phi$ distributions for the azimuthal angle ϕ of **J′** relative to the **k,k′** plane. The simulations were carried out for each of the three limiting cases for the three composite profiles that are dominated by individual bipolar moments, described in the Appendix and listed in Table 2. The previously derived differential cross sections and F_T values from Figure 6 were used in these calculations. Comparisons with the experimental data are given in Figure 10 for the $v'' = 0$, $N'' = 13$ level. The data are now taken for some cases from "differences of differences" (e.g., in Figure 10a the profile is the difference of the (A − D) profiles for the Q and

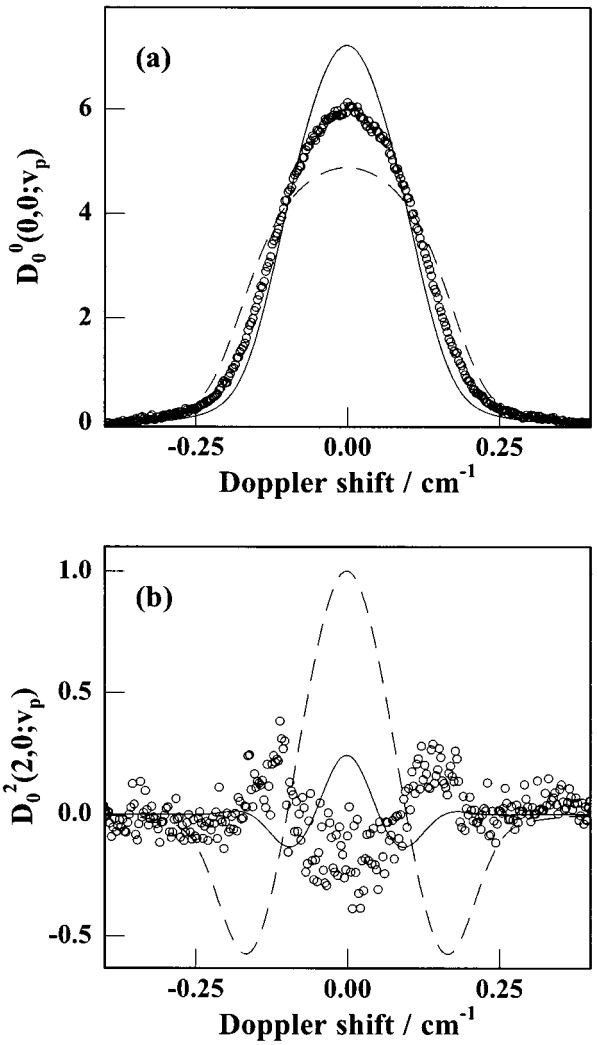

Figure 9. Calculated composite profiles for backward (solid line) and forward (dashed line) scattering for the $v'' = 0$, $N'' = 13$ state compared with the experimental data (circles). For these simulations the distribution of available energy in translation was assumed to be the same as that shown in Figure 6d, and the calculated profiles should be compared with the fits for dominantly sideways scattering shown in parts a and b of Figure 6.

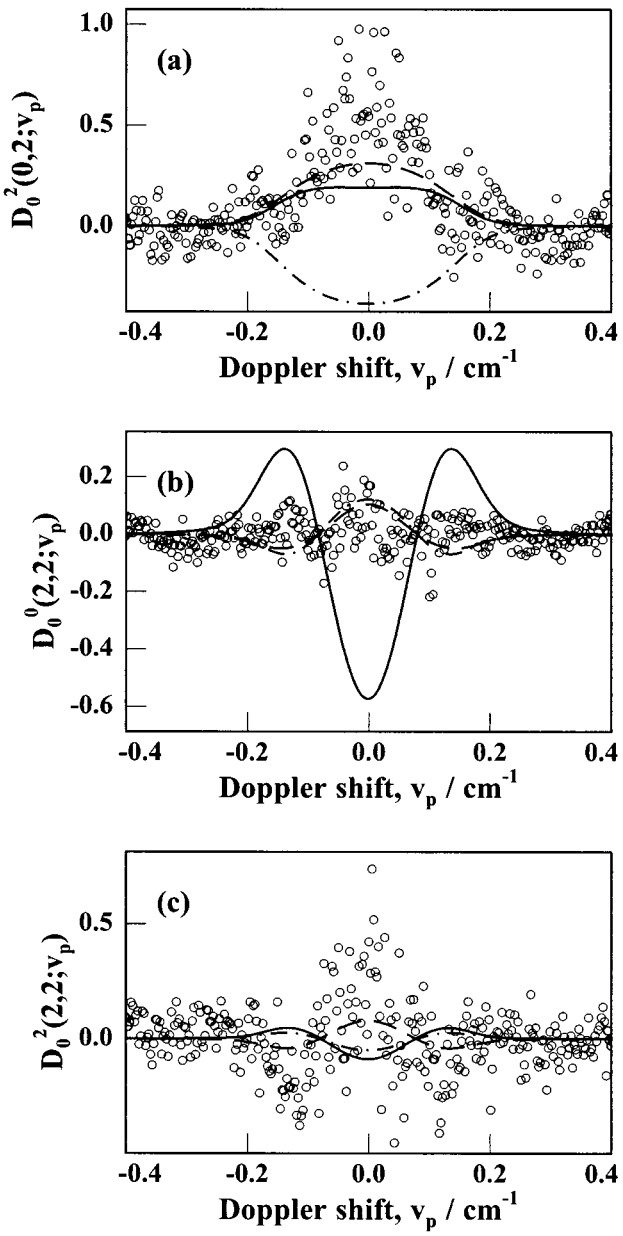

Figure 10. Composite profiles for the $v'' = 0$, $N'' = 13$ data that illustrate angular momentum polarization. Three profiles have been calculated from the data, each having one dominant bipolar moment as described in Appendix. In each of these cases profiles have been calculated for the three limiting types of motion, namely, "frisbee" (dashed line), "propeller" (solid line), and "cartwheel" (dot−dash line). Despite the poor quality of the data, it can be seen that the "frisbee" motion best represents the dynamics.

P branches) and hence are subject to considerable experimental error. Despite the poor experimental quality, it is apparent from the simulations that one of the limiting cases, the frisbee, is much closer to the data than the others. In particular the other two limiting cases both fail conspicuously on one account each, that is, the large $D_0^0(2,2;v_p)$ moment shown by the propeller simulation and the negative $D_0^2(0,2;v_p)$ moment shown by the cartwheel simulation, both absent in the data. The last of these would correspond to a positive LAB frame averaged rotational alignment, which as shown in section V.A is not observed. These simulations thus give us strong evidence to support a frisbee type motion of the product OH in the $v'' = 0$, $N'' = 13$ state. A similar conclusion was drawn for the data of the $v'' = 1$, $N'' = 6$ state.

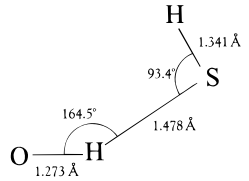

Figure 11. Calculated geometry of the planar transition state in the $O(^3P) + H_2S \rightarrow OH + SH$ reaction, according to ref 42.

VI. Discussion

From the results presented in this and the preceding paper we now attempt to construct a model of the dynamics of the reaction. We first summarize the major findings for the OH product.

1. The reaction produces OH in both $v'' = 0$ and $v'' = 1$, with the rotational distribution in $v'' = 1$ reaching the energetically accessible limit and indicating an efficient conversion of reagent translational energy into OH rotation.[31]

2. There is a preference for formation of OH $v'' = 1$ in the A′ symmetric Λ doublet for all values of N''. There is no significant spin−orbit propensity.[31]

3. Differential cross section measurements on the maximum populated level, $v'' = 1$, $N'' = 6$ showed that for the A″ Λ doublet the scattering was largely sideways/backward, with the remaining energy appearing largely as relative translation, i.e., little rotational excitation in the SH cofragment (Figure 5). Separate measurements that averaged the two Λ doublets showed the same effect, implying that the scattering kinematics appears to be the same for both Λ doublets in this state. For the $v'' = 0$, $N'' = 13$ A′ level the scattering was again sideways/backward peaked with the remaining energy appearing as translational motion. The angular momentum in the OH product indicates that it departs from the transition state like a frisbee. For the rotationless $v'' = 1$, $N'' = 1$ state the results are more equivocal, but if the SH internal energy is assumed to be low (as deduced in the other quantum states), then the OH product is backward-scattered.

Sideways scattering has been observed in a number of molecular beam studies of which two extremes can be considered. The first, exemplified by the $F + C_2H_4$ system, results from the breakup of an oblate symmetric top collision complex, which has lived for many rotational periods.[39] The nonstatistical nature of the rotational[31] and vibrational[40] distributions appears to rule out the possibility of complex formation. Sideways scattering in the direct $O(^3P) + OCS$ reaction has been attributed to side-on attack of the electrophilic O atom on the S followed by recoil along the breaking CS bond.[41] Such attack in the present system might be expected on the HOMO of the S atom, an out-of-plane p type orbital, but this would form a pyramidal transition state that is believed to lead to H + HSO products.[42] Furthermore, the present preference for one of the Λ doublets may indicate a plane of symmetry in the transition state. We thus favor a direct H atom abstraction from a planar transition state from which sideways scattering dominates.

In part 1 we discussed an explanation for the predominance of the A′ Λ doublet in terms of the calculated planar transition state for the reaction,[31] and we now consider if this planar transition state is compatible with the vector correlations described above. Figure 11 shows the calculated geometry of the transition state; the reaction has a barrier such that under the present conditions the majority of the approaching $O(^3P)$ atoms that reach the transition state have their kinetic energy converted into potential energy of the system. The impulse along the breaking S−H bond secures a high rotational energy in OH

and predicts low rotational energy in SH as the impulse passes close to the center of mass of the latter. If the translational energy derives only from the impulse (i.e., that this is large in comparison with the kinetic energy of the O atom in excess of the barrier), then the diatomic fragments will recoil with their relative velocity vector $\mathbf{k}'$ along the line joining their centers of mass, i.e., essentially along the line between the O and S atoms in the transition state. Sideways scattering can be seen to originate from $\mathbf{k}$ vectors (which are largely along the O atom velocity) that lie perpendicular to this line, i.e., from O atom trajectories that are approximately parallel to a line joining the two H atoms in Figure 11. Backward scattering can also be seen to be a possibility, but forward scattering (as might be expected in a direct stripping mechanism) appears unlikely. OH would depart the transition state rotating with the angular momentum vector perpendicular to the scattering plane, the frisbee type motion observed. We see in this highly simplified model that sideways trajectories would be favored over backward because of the larger possible angle of attack of the O atom, but a fuller explanation of the strongly preferred sideways scattering might reflect the steepness of the angular anisotropy of the PES near the transition state.

This simplified model neglects the range of transition states that are possible above the barrier. A more bent transition state (the O−H−S angle smaller than 164.5°) would lead to higher rotational excitation, and since this can only occur for higher energy collisions, it could lead to the efficient mapping of excess kinetic energy into product rotation that is observed. A stripping mechanism might be expected at these higher O atom kinetic energies, which, from the arguments expressed above, would be associated with high ($N'' > 8$) rotational levels in OH($v'' = 1$) and which were not probed in the current experiments. We note that the dynamics of the model would be broadly the same for either Λ doublet; both mechanisms that give rise to A′ and A″ states outlined in part 1 result in repulsion along the S−H bond.

Backward scattering is observed to be favored in the rotationless $N'' = 1$ state of OH($v'' = 1$) if F_T is constrained to the same values as found for higher N'' levels. $N'' = 1$ states would be formed either from a transition state in which the S−H−O atoms are linear or in which H_2S in-plane rotation can compensate for the angular momentum transferred to OH as the SH bond breaks. Backward scattering would be expected for the low proportion of trajectories in which the O atom velocity was along the S−H bond, but this argument would require that trajectories that would appear to sample such a linear configuration from O atom velocities that are not along the S−H bond (and would lead, for example, to sideways scattering) either never reach this transition state because of repulsion or sample instead the bent transition state of Figure 11. Such conclusions, however, are based on assumptions on an interpretation of the $N'' = 1$ data that is not unambiguous.

The model results in predictions for the unobserved SH fragment. First, the rotational energy will be low, but most scattering models in which an impulse is given to a transferred light atom will predict low rotational energy in the remaining fragment. The Λ doublet ratio should favor the asymmetric A″ state as described in part 1.[31] Scattering of SH should be dominantly sideways and forward with respect to the incoming O(^{3}P) atom, with again the frisbee type motion favored. LIF cannot be carried out on the SH fragment because of predissociation of the upper $^2\Sigma^+$ state, but deuterium substitution leads to a high fluorescence quantum yield for rotational levels $N' \lesssim 10$ in $v' = 0$ and would render the observation of the scattering of the cofragment (rarely seen in laser-probed experiments) a possibility.[43]

VII. Conclusions

Doppler resolved LIF on the nascent OH product of the O(^{3}P) + H_2S reaction has been used to study its angular scattering and angular momentum polarization. The broad conclusions are that OH in $v'' = 0$, $N'' = 13$ and in $v'' = 1$, $N'' = 6$ is dominantly sideways/backward scattered, with the remaining energy appearing largely as translational separation of the fragments. Polarization measurements indicate that the OH leaves the transition state with a "frisbee" type motion, its rotational angular momentum vector being perpendicular to the scattering plane. Backward scattering is deduced for the rotationless $v'' = 1$, $N'' = 1$ level, providing the assumption is made that the rotational energy distribution in the SH fragment is similar to that deduced for the other levels. A model invoking a planar transition state is used to explain both these data and the observations of a dominantly A′ Λ doublet propensity and an efficient conversion of high reagent translational energy into OH rotation reported in the previous paper. The model makes predictions about the scattering of the SH coproduct, and experiments designed to probe the more easily detectable SD species from the O + D_2S reaction are planned in this laboratory.

Acknowledgment. We are grateful to the EPSRC for support of this work through the provision of studentships (M.L.C. and G.A.D.R.).

Appendix

We consider here the simulation of a Doppler profile appropriate to the OH product of the O(^{3}P) + H_2S reaction, where O(^{3}P) is formed from the polarized photodissociation of NO_2. In common with Brouard et al.[6] we first define three frames of reference. These are the laboratory (LAB) frame, in which the electric vector of the photolysis laser forms the z axis and in which the hot atom A has a velocity $\mathbf{v_A}(v_A,\theta_A,\phi_A)$ with an angular dependence defined by the photodissociation of NO_2. The overall hot atom velocity distribution, allowing for possible internal energy in the NO cofragment and for the effect of the thermal motion of the precursor, can be written as[44]

$$I(v_A,\theta_A) = \frac{A(v_A)}{4\pi}[1 + \beta_{v_A}(v_A)P_2(\cos\theta_A)] \qquad \text{(A1)}$$

where $A(v_A)$ is the speed distribution and $\beta v_A(v_A)$ is an (speed-dependent) anisotropy parameter for the 355 nm dissociation of NO_2. The target molecule BCD has a Maxwell−Boltzmann velocity distribution $\mathbf{v_{BCD}}(v_{BCD},\theta_{BCD},\Phi_{BCD})$, and we can calculate the velocity of the center of mass $\mathbf{v_{CM}} = \gamma\mathbf{v_A} + (1 - \gamma)\mathbf{v_{BCD}}$ where $\gamma = m_A/(m_A + m_{BCD})$. The second frame of reference is the "moving" frame and is referenced to the hot atom velocity, which forms the z axis of the system, with the zx plane defined as that in which $\mathbf{v_A}$ and $\mathbf{v_{CM}}$ lie. Finally, we have the center of mass (CM) frame. This is referenced to the relative collision velocity $\mathbf{k} = \mathbf{v_A} - \mathbf{v_{BCD}}$, with the positive z direction being in the direction of motion of the hot atom, and the product scatters in this frame with a velocity $\mathbf{u}(u,\theta_u,\phi_u)$. The zx plane is defined as that in which $\mathbf{k}$ and $\mathbf{k}'$ lie, and the azimuthal scattering angle ϕ_u is then defined as the angle between the CM frame zx plane and the moving frame zx plane, with the convention that the angle is positive for rotation of the CM zx plane away from the moving frame zx plane. The polar angle that separates $\mathbf{v_A}$ and $\mathbf{k}$ is defined as θ_k, while the polar

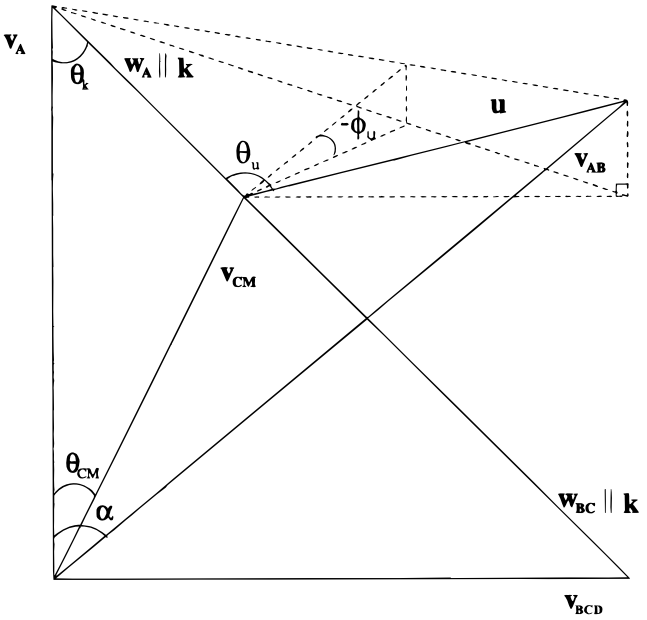

Figure 12. Vectors and angles relating the frames of reference explained in the text.

angle that separates $\mathbf{v_A}$ and $\mathbf{v_{CM}}$ is defined as θ_{CM}. The various vectors and the angles that relate them are shown in Figure 12.

The vector shown as $\mathbf{v_{AB}}$ may be written in terms of the various LAB and CM frame vectors using the cosine rule and the spherical harmonic addition theorem.[45] This yields the following expressions

$$v_{AB}{}^2 = u^2 + v_{CM}{}^2 + 2uv_{CM}[\cos\theta_u \cos(\theta_k + \theta_{CM}) + \sin\theta_u \sin(\theta_k + \theta_{CM}) \cos\phi_u] \quad \text{(A2)}$$

$$\cos\alpha = \frac{v_{AB}{}^2 + v_A{}^2 - u^2 - w_A{}^2 + 2uw_A \cos\theta_u}{2v_{AB}v_A} \quad \text{(A3)}$$

where

$$w_A{}^2 = v_A{}^2 + v_{CM}{}^2 - 2v_A v_{CM} \cos\theta_{CM} \quad \text{(A4)}$$

These relations give us the velocity of the product in the moving frame in terms that depend only on the known starting velocities in the LAB frame, the masses of the reagents and products and the scattering information we seek (primarily θ_u). In the limit where $\mathbf{v_A} \gg \mathbf{v_{BC}}$ the angles θ_k and θ_{CM} tend to zero and the above results tend to those derived by Shafer et al.[23]

Construction of Doppler Profiles. The velocity of the product, $\mathbf{v_{AB}}$, in the moving frame can thus be calculated for known starting conditions and scattering dynamics. The Doppler profiles will be dependent on the correlated distribution of translation and rotation of the product, as first shown by Dixon for photodissociation[46] and later extended to reactive systems.[6,10] The distribution in the moving frame can be expressed as an expansion in bipolar harmonics and then rotated into the LAB frame to give the result shown in eq 2 of the text.

The angular momentum dependent bipolar moments can be removed by forming linear combinations of profiles from different rotational branches and experimental geometries, and the various combinations used in this paper are listed in Table 2 along with the resulting expressions for the composite profiles thus created. The two composite profiles formed that are independent of the angular momentum are given as $D_0^0(0,0;v_p)$ and $D_0^2(2,0;v_p)$. These form respectively a "top-hat" profile dependent purely on the speed of the product in the moving frame, which is the same as that in the LAB frame, and a profile whose width is dependent on the speed and whose shape is dependent on an anisotropy parameter that is labeled $\beta v_A v_{AB}(v_{AB})$. This anisotropy parameter is simply the second-order Legendre polynomial $P_2(\cos\alpha)$, where $\cos\alpha$ has been defined in eq A3 and depends on the CM scattering angle θ_u. We can thus form composite Doppler profiles that are dependent on the moving frame velocity derived via eqs A1−A4 for any arbitrary center-of-mass speed and scattering angle provided we know the initial velocities of the reagents.

Angular Momentum Correlations. In the classical limit, for each scattering event we may consider the angular momentum vector, $\mathbf{J}(J,\theta_J,\phi_J)$, to be pointing into some solid angle $\sin\theta_J\, d\theta_J\, d\phi_J$ in the CM frame. This may be rotated into the moving frame by application of the Cartesian rotation matrices,[45] using the Euler angles that relate the two frames, namely, $(-\phi_u, \theta_k, 0)$. This yields a new angular momentum vector $\mathbf{J'}(J',\theta_J',\phi_J')$ referenced to the moving frame axes. The Doppler profiles are sensitive to the moving frame bipolar moments, which may be generated using the functions given in Table 2 of ref 46. The angular momentum dependent bipolar moments may be isolated in the same fashion as those describing the differential scattering cross section, and the three resulting composite Doppler profiles are also listed in Table 2.

References and Notes

(1) Lee, S. H.; Liu, K. P. *J. Phys. Chem. A* **1998**, *102*, 8637.
(2) Hsu, Y.-T.; Liu, K. *J. Chem. Phys.* **1997**, *107*, 1664.
(3) Wang, J.-H.; Liu, K.; Schatz, G. C.; ter Horst, M. *J. Chem. Phys.* **1997**, *107*, 7869.
(4) Lee, S. H.; Liu, K. P. *Chem. Phys. Lett.* **1998**, *290*, 323.
(5) Green, F.; Orr-Ewing, A. J.; Hancock, G. *Faraday Discuss. Chem. Soc.* **1991**, *91*, 79.
(6) Aoiz, F. J.; Brouard, M.; Enriquez, P. A.; Sayos, R. *J. Chem. Soc., Faraday. Trans.* **1993**, *89*, 1427.
(7) Brouard, M.; Lambert, M. H.; Russell, C. L.; Short, J.; Simons, J. P. *Faraday Discuss. Chem. Soc.* **1995**, *102*, 179.
(8) Brouard, M.; Lambert, M. H.; Short, J.; Simons, J. P. *J. Phys. Chem.* **1995**, *99*, 13751.
(9) Brouard, M.; Duxon, S. P.; Enriquez, P. A.; Sayos, R.; Simons, J. P. *J. Phys. Chem.* **1991**, *95*, 8169.
(10) Costen, M. L.; Hancock, G.; Orr-Ewing, A. J.; Summerfield, D. *J. Chem. Phys.* **1994**, *100*, 2754.
(11) Kim, H. L.; Wickramaaratchi, M. A.; Zheng, X.; Hall, G. E. *J. Chem. Phys.* **1994**, *101*, 2033.
(12) Fei, R.; Zheng, X. S.; Hall, G. E. *J. Phys. Chem. A* **1997**, *101*, 2541.
(13) Brouard, M.; Lambert, H. M.; Rayner, S. P.; Simons, J. P. *Mol. Phys.* **1996**, *89*, 403.
(14) Brouard, M.; Burak, I.; Markillie, G. A. J.; McGrath, K.; Vallance, C. *Chem. Phys. Lett.* **1997**, *281*, 97.
(15) Alexander, A. J.; Aoiz, A. J.; Brouard, M.; Short, J.; Simons, J. P. *Isr. J. Chem.* **1997**, *37*, 317.
(16) Brouard, M.; Burak, I.; Gatenby, S. D.; Markillie, G. *Chem. Phys. Lett.* **1998**, *287*, 682.
(17) Brouard, M.; Hughes, D. W.; Kalogerakis, K. S.; Simons, J. P. *J. Phys. Chem. A* **1998**, *102*, 9559.
(18) Alexander, A. J.; Aoiz, F. J.; Brouard, M.; Burak, I.; Fujimura, Y.; Short, J.; Simons, J. P. *Chem. Phys. Lett.* **1996**, *262*, 589.
(19) Alexander, A. J.; Aoiz, F. J.; Bañares, L.; Brouard, M.; Short, J.; Simons, J. P. *J. Phys. Chem. A* **1997**, *102*, 7544.
(20) Alexander, A. J.; Blunt, D. A.; Brouard, M.; Simons, J. P.; Aoiz, F. J.; Beñares, L.; Fujimura, Y.; Tsubouchi, M. *Faraday Discuss. Chem. Soc.* **1997**, *108*, 375.
(21) Simpson, W. R.; Orr-Ewing, A. J.; Rakitzis, T. P.; Kandel, S. A.; Zare, R. N. *J. Chem. Phys.* **1995**, *103*, 7299. Simpson, W. R.; Orr-Ewing, A. J.; Rakitzis, T. P.; Kandel, S. A.; Zare, R. N. *J. Chem. Phys.* **1995**, *103*, 7313.
(22) Schafer, N. E.; Orr-Ewing, A. J.; Zare, R. N. *Chem. Phys. Lett.* **1993**, *212*, 163.
(23) Schafer, N. E.; Orr-Ewing, A. J.; Simpson, W. R.; Xu, H.; Zare, R. N. *Chem. Phys. Lett.* **1993**, *212*, 155.
(24) Orr-Ewing, A. J.; Simpson, W. R.; Rakitzis, T. P.; Kandel, S. A.; Zare, R. N. *J. Chem. Phys.* **1997**, *106*, 5961.

(25) Simpson, W. R.; Rakitzis, T. P.; Kandel, S. A.; Lev-On, T.; Zare, R. N. *J. Phys. Chem.* **1996**, *100*, 7938.

(26) Kandel, S. A.; Rakitzis, T. P.; Lev-On, T.; Zare, R. N. *J. Phys. Chem. A* **1998**, *102*, 2270.

(27) Kandel, S. A.; Zare, R. N. *J. Chem. Phys.* **1998**, *109*, 9719.

(28) Orr-Ewing, A. J.; Zare, R. N. Orientation and alignment of the products of bimolecular reactions. In *Chemical Dynamics and Kinetics of Small Radicals*; Wagner, A., Liu, K., Eds.; World Scientific: Singapore, 1994.

(29) Schafer-Ray, N. E.; Orr-Ewing, A. J.; Zare, R. N. *J. Phys. Chem.* **1995**, *99*, 7591.

(30) Aoiz, F. J.; Brouard, M.; Enriquez, P. A. *J. Chem. Phys.* **1996**, *105*, 4964.

(31) Costen, M. L.; Hancock, G.; Ritchie, G. A. D. *J. Phys. Chem. A* **1999**, *103*, 10644.

(32) Docker, M. P. *Chem. Phys.* **1989**, *135*, 405.

(33) Jansson, P. A. *J. Opt. Soc. Am.* **1970**, *60*, 184.

(34) Press, W. H.; Flannery, B. P.; Teulokolsky, S. A.; Vetterling, W. T. *Numerical Recipies*; Cambridge University Press: Cambridge, 1986.

(35) Balucani, N.; Beneventi, L.; Casavecchia, P.; Stranges, D.; Volpi, G. G. *J. Chem. Phys.* **1991**, *94*, 861.

(36) Dieke, G. H.; Crosswhite, H. M. *J. Quant. Spectrosc. Radiat. Transfer* **1962**, *2*, 97.

(37) Costen, M. L. Ph.D. Thesis, Oxford University, 1997.

(38) Davidson, F. E.; Clemo, A. R.; Duncan, G. L.; Bowett, R. J.; Dobson, J. H.; Grice, R. *Mol. Phys.* **1982**, *46*, 33.

(39) Parson, J. M.; Shobatake, K.; Lee, Y. T.; Rice, S. A. *Faraday Discuss. Chem. Soc.* **1973**, *55*, 344.

(40) Agrawaller, B. S.; Setser, D. W. *J. Chem. Phys.* **1987**, *86*, 5421.

(41) Rochford, J. J.; Powell, L. J.; Grice, R. *J. Phys. Chem.* **1995**, *99*, 15369.

(42) Goumri, A.; Laakso, D.; Rocha, J.-D, R.; Smith, C. E.; Marshall, P. *J. Chem. Phys.* **1995**, *102*, 161.

(43) Friedl, R.; Brune, W. H.; Anderson, J. G. *J. Chem. Phys.* **1983**, *79*, 4227.

(44) Zare, R. N. *Mol. Photochem.* **1972**, *4*, 1.

(45) Zare, R. N. *Angular Momentum: Understanding Spatial Aspects in Chemistry and Physics;* Wiley: New York, 1988.

(46) Dixon, R. N. *J. Chem. Phys.* **1986**, *85*, 1866.